Journal of Computational Physics 229 (2010) 8031–8044

Contents lists available at ScienceDirect

Journal of Computational Physics

journal homepage: www.elsevier.com/locate/jcp

Heuristic optimality criterion algorithm for shape design of fluid flow

Limin Wang [a,b], Yilin Fan [a], Lingai Luo [a,*]

[a] Laboratoire Optimisation de la Conception et Ingénierie de l'Environnement (LOCIE), CNRS-FRE 3220, Université de Savoie, Polytech' Annecy-Chambéry, Campus Scientifique, Savoie Technolac, 73376 Le Bourget-Du-Lac Cedex, France
[b] State Key Laboratory of Multiphase Complex Systems, Institute of Process Engineering, Chinese Academy of Sciences, Beijing 100190, China

ARTICLE INFO

Article history:
Received 1 May 2009
Received in revised form 4 June 2010
Accepted 1 July 2010

Keywords:
Shape design
Heuristic optimality criterion
Lattice Boltzmann method
Fluid flow
Pressure drop

ABSTRACT

This paper presents a heuristic optimality criterion algorithm for shape design of fluid flow. In this algorithm, the lattice Boltzmann method (LBM) is utilized to calculate the flow field of a fluid domain which is divided into elemental cells. A heuristic optimality criterion is applied for cells at the solid–fluid interface, i.e. the dynamic pressure for fluid cells and the viscous stress on their neighboring solid cells. An automatic program is processed step by step to exchange the positions of solid and fluid cells identified by the optimality criterion, with the objective of decreasing the flow resistance at the constraint of constant fluid volume. To illustrate the procedure of this algorithm for shape design of fluid flow, two simple examples are presented: one with fluid flowing through a right angle elbow and the other through a converging *T*-junction. Numerical results show that this algorithm can successfully reduce the total pressure drop of the system, demonstrating its potential applications in engineering optimal design.

1. Introduction

When fluid flows through a channel or a tube, the friction between fluid and solid wall causes pressure drop or viscous dissipation. How to effectively reduce this viscous dissipation by proper design of channel shape or flow system configuration, i.e. shape optimization of fluid flow is essential to many engineering applications involving fluid, such as aerodynamic wing and wing-body configurations [1], fluid distributors [2–4], and air distribution system in a vehicle [5,6]. The detailed review on shape optimization of fluid flow may be found in some monographs and papers [7–10]. In recent years, a great deal of effort has been devoted to the development of numerical technique for solving the flow optimization issue. Borrvall and Petersson [11] first applied the topology optimization well established in solids and structures to the optimal design in fluid mechanics. They proposed the optimal design of Stokes flow problems by distributing inhomogeneous porous materials with a spatially varying Darcy permeability tensor and an artificial "inverse permeability" that is proportional to the elemental thickness of a two-dimensional channel. This approach is extended by Evgrafov [12] to pure solid and pure flow, and by Gersborg-Hansen et al. [13] to laminar incompressible Navier–Stokes flows at low Reynolds numbers, higher than that of the Stokes flow. Evgrafov [14] further proposed to relax the incompressibility constraint, and applied the topology optimization for slightly compressible Navier–Stokes flows. More recently, Evgrafov and his coworkers [15,16] combined the variation of the porosity with LBM for topology optimization of low Mach number incompressible viscous flows, which mainly applied the LBM as an alternative to Navier–Stokes equation solvers. Moos and his coworkers [5,6] proposed a procedure for topology optimization of fluid flow, which is mainly based on the principle that the fluid flow always searches the best way under given constraints in a predefined space by itself. In their algorithm, the areas are responsible for the bulk of pressure loss

* Corresponding author. Tel.: +33 479758193; fax: +33 479758144.
E-mail address: Lingai.LUO@univ-savoie.fr (L. Luo).

0021-9991/$ - see front matter © 2010 Elsevier Inc. All rights reserved.
doi:10.1016/j.jcp.2010.07.006

Nomenclature

$\mathbf{c}$	particle velocity, LT^{-1}
c_s	speed of sound, LT^{-1}
Δp	pressure drop, $L^{-1}MT^{-2}$
Nx	lattice number in x direction, dimensionless
Ny	lattice number in y direction, dimensionless
Re	Reynolds number, dimensionless
Re_{out}	Reynolds number at outlet, dimensionless
ω_i	lattice weighting factor, dimensionless
$\mathbf{u}$	macroscopic velocity, LT^{-1}
μ	fluid viscosity, $L^{-1}MT^{-1}$
v	kinematic viscosity, L^2T^{-1}
ρ	density, $L^{-3}M$
ρ_0	mean density, $L^{-3}M$
W_{in}	width of inlet, L
W_{out}	width of outlet, L
τ_{yx}	shear stress in x direction, $L^{-1}MT^{-2}$
τ_{xy}	shear stress in y direction, $L^{-1}MT^{-2}$
δx	lattice spacing in x direction, L
δy	lattice spacing in y direction, L
δt	time interval, T
t	time step, T
f_i	particle distribution functions, dimensionless
f_i^{eq}	particle equilibrium distribution function, dimensionless
τ	relaxation time, T
$\mathbf{x}$	particle position, L
u	velocity in x direction, LT^{-1}
u_{in}	velocity of inlet, LT^{-1}
$\bar{u}_{out}$	cross-sectional average fluid velocity of outlet, LT^{-1}
$\bar{u}$	cross-sectional average fluid velocity, LT^{-1}
v	velocity in y direction, LT^{-1}
p	pressure of fluid, $L^{-1}MT^{-2}$
q	dynamic pressure of fluid, $L^{-1}MT^{-2}$

Acronyms

BGK	Bhatnagar–Gross–Krook
CA	cellular automata
D2Q9	two-dimensional 9-velocity lattice Boltzmann model
D3Q15	three-dimensional 15-velocity lattice Boltzmann model
D3Q19	three-dimensional 19-velocity lattice Boltzmann model
D3Q27	three-dimensional 27-velocity lattice Boltzmann model
EGM	entropy generation minimization
LBM	lattice Boltzmann method
LGA	lattice-gas automata

within the design space so called ‘‘virtual sand” or ‘‘numerical sand” which is deposited in computational cells with recirculation. Duan et al. [17] applied variational level set method for shape-topology optimization of Navier–Stokes flow, where the Gateaux shape derivative was used to analyze the sensitivity of the objective function. Similar problem was also treated by Zhou and Li [18] with the constraint of a specific fluid volume.

Lattice Boltzmann method (LBM) is a relatively new simulation technique for complex fluid domains, which simulates fluids at a more fundamental, or kinetic level via the discrete Boltzmann equation. Some foundational work of LBM is discussed in the monographs and papers [19–25]. Compared to traditional numerical schemes based on discretizations of macroscopic continuum equations, the kinetic nature and local dynamics of the LBM make it more adaptable in dealing with complex boundaries and parallelization of the algorithm. As a result, we envisage applying it as an underlying Navier–Stokes solver which provides flow field information for our heuristic optimality criterion and the following cells' position exchanging process. Shape optimization of fluid flow domain is expected by applying this algorithm for reduced pressure drop (reduced flow resistance) with constraint of constant void volume for fluid flow. In fact, the LBM was originally derived as an extension of the Lattice Gas Automata (LGA) which originated from Cellular Automata (CA) method [26]. The theoretical

basis ("cell" expression) of the LBM corresponds very well to the downstream position exchanging process. That is the reason why we choose the LBM as the "pretreatment".

The outline of this paper is as follows. In Section 2, cellular expression for fluid–solid structures and the dynamical interaction at fluid–solid interface are presented. A description of the LBM, the heuristic optimality criterion, and the coupled algorithm is given as well. Section 3 demonstrates the success of this algorithm for shape design of fluids flowing through a right angle elbow and a converging *T*-junction subject to a specific fluid volume constraint. Finally, Section 4 summarizes some conclusions and presents remarks.

2. Numerical algorithm

Here we give the theoretical background for the numerical algorithm. First we specify our dynamical model for the interaction at fluid–solid interface, and then we describe the simulation rules used for our system, i.e., the LBM, the heuristic optimality criterion, and the coupled algorithm.

To simplify the numerical algorithm, following assumptions are made:

- Steady flow pattern; No-slip condition at the wall is applied.
- The simulation is restricted to a two-dimensional domain. The height of the channel is infinite, thus only the friction between the fluid and the solid walls at both sides are considered.
- The gravity effect of the fluid is neglected.
- The operation condition is isothermal, i.e. neglecting the viscous heating effect.
- Physical properties of solid materials are isotropic and homogeneous; Physical properties of working fluid are constant.

2.1. Cellular expression for fluid–solid structures

As shown in Fig. 1, the simulation domain is uniformly divided into elemental square sub-domains, which are considered as cells. The solid cells are indicated by black and the fluid cells represented by yellow, respectively. The physical information of cells on the whole domain is calculated by the LBM.

In fluid phase, we use the D2Q9 model [24] with three speeds and nine velocities on a two-dimensional square lattice (Fig. 2). The velocities, $\mathbf{c}_i$, include eight moving velocities along the links of the square lattice and a zero velocity for the rest particle. Let $f_i(\mathbf{x},t)$ be the distribution functions at $\mathbf{x}$, t with velocity $\mathbf{c}_i$, the lattice Boltzmann equation with the BGK collision approximation [24] can be written as

$$f_i(\mathbf{x}+\mathbf{c}_i\delta t, t+\delta t) = f_i(\mathbf{x},t) - \frac{1}{\tau}\left(f_i - f_i^{eq}\right), \tag{1}$$

where f_i^{eq} $(i = 0,1,\ldots,8)$ is the equilibrium distribution function and τ is the relaxation time.

For low Mach number flow conditions, the equilibrium distribution function for the D2Q9 model in Eq. (1) can be derived by a Taylor series 2nd order expansion of the Maxwell–Boltzmann equilibrium distribution, as the following [21]:

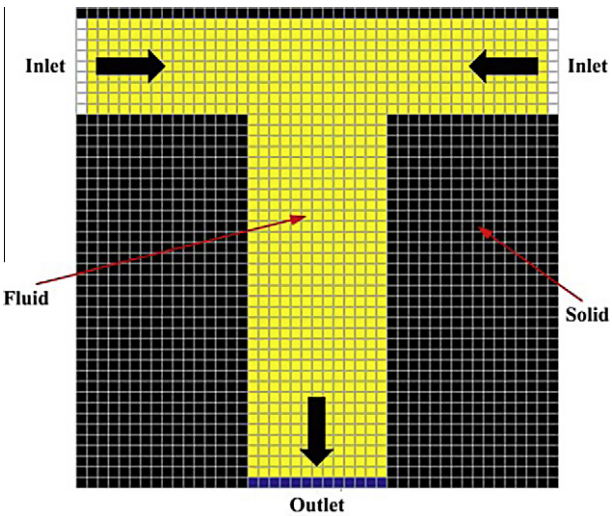

Fig. 1. Schematic of the cellular expression for the simulation domain.

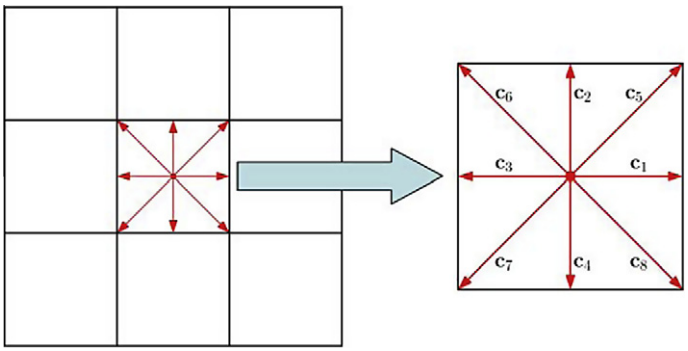

Fig. 2. A two-dimensional (2D), 9-velocity D2Q9 lattice model.

$$f_i^{eq} = \rho\omega_i\left[1 + 3\mathbf{c}_i\cdot\mathbf{u} + \frac{9}{2}(\mathbf{c}_i\cdot\mathbf{u})^2 - \frac{3}{2}\mathbf{u}\cdot\mathbf{u}\right], \tag{2}$$

where $\mathbf{u}$ is the macroscopic velocity, and ω_i is the lattice weighting factor that depends on the lattice geometry. For the square lattice these weights are:

$$\omega_i = \begin{cases} 4/9 & i = 0, \\ 1/9 & i = 1,2,3,4, \\ 1/36 & i = 5,6,7,8. \end{cases} \tag{3}$$

The macroscopic quantities such as mass density and momentum density can then be obtained by evaluating the hydrodynamic moments of the distribution function $f_i(\mathbf{x},t)$ by

$$\rho(\mathbf{x},t) = \sum_{i=0}^{8} f_i(\mathbf{x},t), \tag{4}$$

$$\rho\mathbf{u}(\mathbf{x},t) = \sum_{i=0}^{8} \mathbf{c}_i f_i(\mathbf{x},t). \tag{5}$$

For the D2Q9 model, the lattice speed or lattice constant is defined as $c = \delta x/\delta t$, δx and δt are the lattice spacing and the time step size, respectively. The speed of sound in D2Q9 lattice model is $c_s = c/\sqrt{3}$ and the equation of state is that of an ideal gas,

$$p = \rho c_s^2. \tag{6}$$

Under the low Mach number assumption, the familiar form of incompressible Navier–Stokes equations can be recovered from the incompressible lattice Boltzmann model via the Chapman–Enskog expansion [23], as the following

$$\frac{1}{c_s^2}\frac{\partial P}{\partial t} + \nabla\cdot\mathbf{u} = 0, \tag{7}$$

$$\frac{\partial\mathbf{u}}{\partial t} + \mathbf{u}\cdot\nabla\mathbf{u} = -\nabla P + \nu\nabla^2\mathbf{u}, \tag{8}$$

where $P = p/\rho_0$, the constant ρ_0 is the mean density and the kinematic viscosity

$$\nu = \frac{(2\tau - 1)}{6}\frac{\delta x^2}{\delta t}. \tag{9}$$

These works guarantee that the Navier–Stokes equation can be obtained at a macroscopic level. We apply the LBM to calculate the physical quantities of microscopic and mesoscopic process in fluid cells.

2.2. Dynamical interaction at fluid–solid interface and heuristic criterion

According to the Newton's law of viscosity, we can obtain the fundamental relation for fluid shear stress in the form

$$\tau_{yx} = -\mu\frac{\partial u}{\partial y}. \tag{10}$$

Here, the constant μ is known as the coefficient of viscosity. Some typical fluid–solid interfaces in two-dimensional simulation are indicated in Fig. 3, the solid cell suffers viscous stress force because of fluid flow. At the wall, the velocity is zero owing to the no-slip condition for viscous fluid flows. Therefore, the dynamical interaction between a fluid cell and a solid cell can be written as

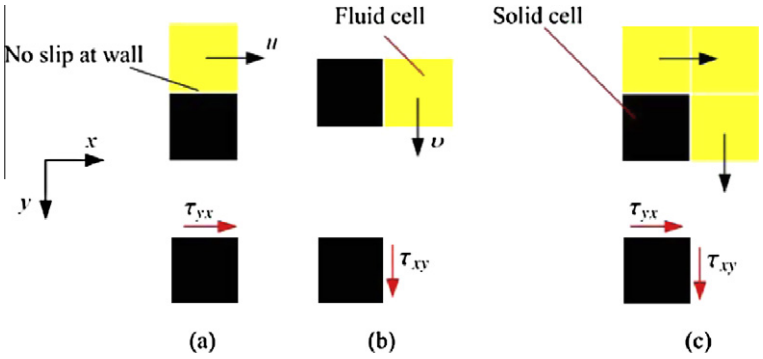

Fig. 3. Some typical fluid–solid interfaces in two-dimensional simulation.

$$\tau_{yx} = \mu \frac{u}{0.5\delta y}, \tag{11}$$

$$\tau_{xy} = \mu \frac{\upsilon}{0.5\delta x}, \tag{12}$$

where δx and δy are the lattice spacing ($\delta x = \delta y$ in the LBM), u and υ are velocity in x and y direction, respectively.

In the view point of solid, material and fracture mechanics, the solid cell collapses when it suffers viscous stress greater than the fracture threshold [27]. Assuming that the physical properties of solid materials are isotropic and homogeneous, the solid cells suffering larger viscous stress from its neighboring fluid cells will be more likely to crash than those suffering small viscous stress, similar to the natural phenomenon of fluvial erosion in river basins. As a result, by using the flow field provided by the LBM we can screen out those solid cells at fluid–solid interface which are liable to perish and vanish due to larger viscous stress, and will be replaced by fluid cells. For simplicity of implementation, the physical properties of solid materials presented here are assumed to be isotropic and homogeneous; however, its extension to anisotropic and inhomogeneous is in principle feasible.

For the fluid phase, recall that only the volume of the flow domain is constrained. In order to eliminate the "dead zones" in the fluid domain so as to effectively make use of a fixed void volume for fluid flow, we choose the dynamic pressure ($q = \frac{1}{2}\rho v^2$) as the heuristic criterion for fluid cells. That is, fluid cells at the fluid–solid interface having lower dynamic pressure are liable to perish and vanish and will be replaced by solid cells. The algorithm proposed by us can then be thought of as a mimicry of natural behavior in channels where the surface is eroded at the points of maximum shear stress and the sand is deposited at the points of minimum dynamic pressure.

To realize the mutual replacement of fluid and solid cells with their proper criteria, i.e. dynamic pressure for fluid cells and viscous stress for solid cells, an automatic procedure is programmed.

2.3. Implementation of the simulation procedure

The simulation procedure is described in detail using the flow chart shown in Fig. 4.

(1) Input the initial data such as the size and initial shape of the simulation domain (solid phase, fluid phase), the specified boundary conditions (fluid nature, velocity profile, pressure, etc.). The fluid density and kinematic viscosity given in this paper are $\rho = 1.0$ and $v = 0.04$, respectively. The initial condition is the equilibrium distribution, using a constant density $\rho_0 = 1.0$ and zero velocity. The wall boundary condition given in this paper is the bounce-back scheme [28–30], which is adaptable, robust and easy to implement for fluid flow in complicated geometries.

(2) An exact flow field is calculated by LBM. The steady-state is reached if

$$\frac{\sum_i \sum_j (|u(i,j,t+\delta t) - u(i,j,t)| + |\upsilon(i,j,t+\delta t) - \upsilon(i,j,t)|)}{\sum_i \sum_j (|u(i,j,t)| + |\upsilon(i,j,t)|)} \leqslant Tol_{LBM}, \tag{13}$$

where Tol_{LBM} is a tolerance set to 10^{-8}.

(3) At the fluid–solid interface, a number of fluid cells having the lowest dynamic pressure and the same number of solid cells suffering the largest viscous stress will be screened out, and their positions will be exchanged, thus creating a new shape. Note that the equal number of the target fluid cells and solid cells is to balance the void volume occupied by fluid (constant fluid volume constraint). In strict sense, only one couple of cells should be exchanged at each step. However, that will by far lengthen the simulation time thus not highly efficient. Therefore, a certain number of fluid–solid cell

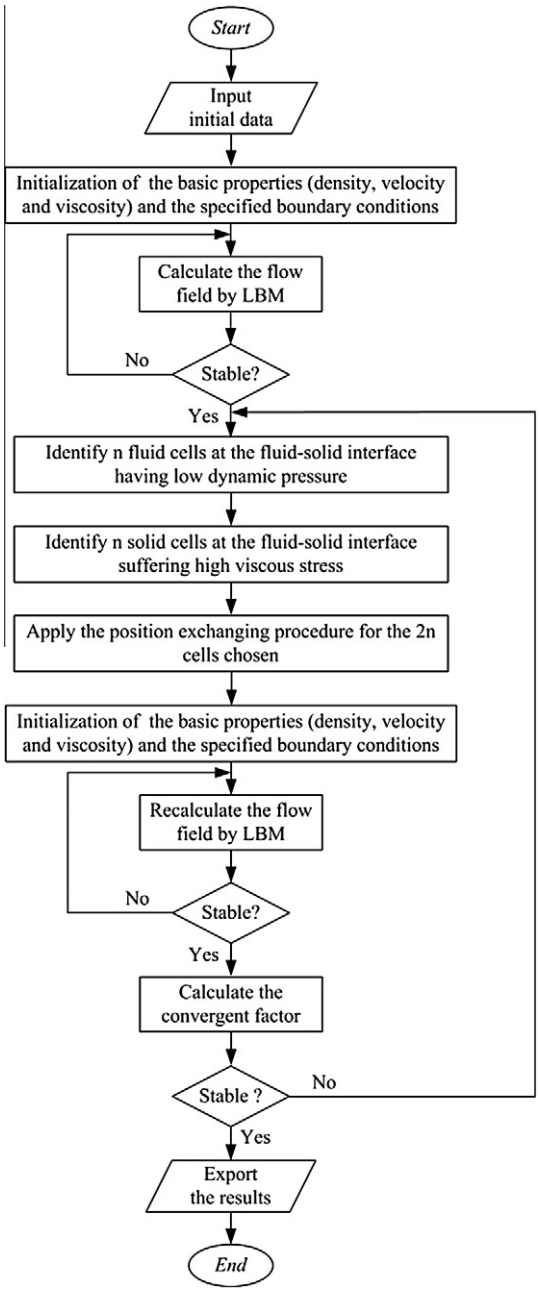

Fig. 4. Flow chart of the algorithm.

couples are exchanged at each step. We introduce here a control parameter called the exchange rate, defined as the ratio of the number of exchanging cells to the total number of cells at the fluid–solid interface. Within the allowable simulation time range, the value of the exchange rate should be necessarily small to encourage convergence of the method. In the presented algorithm, the value of the exchange rate for each step is largely less than 0.05, and excessive exchange rate maybe lead to the failure of the algorithm. The exchange rate given in this paper is 0.04. Note that even low exchange number would be better in some symmetry cases (*T*-junction for example) to ensure the symmetry of the fluid domain.

(4) Reinitialize the basic properties of fluid flow and boundary for the new shape. The whole cells are again initialized by the equilibrium distribution using a constant density $\rho_0 = 1.0$, and zero velocity. Recalculate the exact flow field by LBM.

(5) Check the stable tolerance of the algorithm. If the tolerance is satisfied, then the heuristic procedure is terminated, and the results are exported. If not so, the procedure goes back to Step 3 for recurrence.
The result is considered to be stable when the pressure drop Δp across the system tends to extremum. Owing to the difficulty of absolute convergence toward a specific static pattern, n-step average of Δp is considered as convergent factor, and the result is convergent if

$$\frac{\left|\frac{1}{n\delta t}\sum_{i=t}^{t+n\delta t}\Delta p_i - \frac{1}{n\delta t}\sum_{i=t-n\delta t}^{t}\Delta p_i\right|}{\left|\frac{1}{n\delta t}\sum_{i=t-n\delta t}^{t}\Delta p_i\right|} = \frac{\left|\sum_{i=t}^{t+n\delta t}\Delta p_i - \sum_{i=t-n\delta t}^{t}\Delta p_i\right|}{\left|\sum_{i=t-n\delta t}^{t}\Delta p_i\right|} \leqslant Tol, \tag{14}$$

where Tol is a tolerance set to 10^{-6} and n the length of average step interval, usually from 5 to 10.

3. Simulation and results

In order to test the validity of this algorithm for shape design of fluid flow, we consider two simple examples, both restricted in a two-dimensional domain with $Nx \times Ny$ lattice cells.

3.1. Flow through a right angle elbow

Fluid flowing through a bend or curve in a pipe always induces an energy loss larger than the simple straight-pipe skin friction loss, due to singular effect from the centripetal acceleration. Fig. 5 shows the arrangement of simulation domain, which is divided into 200×200 cells. The width of both inlet and outlet is $W_{in} = W_{out} = 40$ cells. The parabolic velocity profiles at both inlet and outlet are imposed. The cross-sectional average fluid velocities of both inlet and outlet are $\bar{u} = 0.0000267, 0.02, 0.04$ and 0.08, the corresponding Reynolds numbers $Re = \frac{\bar{u}W_{in}}{\nu} = 0.0267, 20, 40$ and 80.

Fig. 6 shows the evolution of shape and flow field as a function of the evolution time steps for $Re = 40$. With the algorithm proceeds, the flow singularity (right angle) gradually despairs and becomes smoother, implying that the singularity effect is smaller and smaller. Finally, it reaches a relative steady-state, i.e. the shape of fluid flow almost does not change as time step increases. It can be observed that the streamline of velocity profile is well-kept at the final shape so that the flow turns slowly and continuously rather than abruptly.

The pressure drop of the system as a function of evolution time step is indicated in Fig. 7, where the objective values are given in lattice units. The total pressure drop of the initial shape is 0.0894, that of the final shape is 0.0279, thus the total pressure drop of the final shape is reduced by 68.8% compared with that of the initial shape. It can be observed that the pressure drop globally decreases when the shape of fluid flow evolves with increasing time step, and tends to be stable after having been reduced to a certain level. However, the local fluctuation characteristics of pressure drop occur during the evolution, which can be understood as reflections of spatio-temporal coupling of the flow behaviors to realize the compromise between vanishing solid cells and vanishing fluid cells [31].

From the view point of fluid mechanics, the pressure drop in a pipe is caused by skin friction and singularity effect, namely regular pressure drop and singular pressure drop, respectively. The total pressure drop is the sum of the two parts. The simulation results show that the total pressure drop is decreased 68.8% by reducing the flow singularity effect, implying

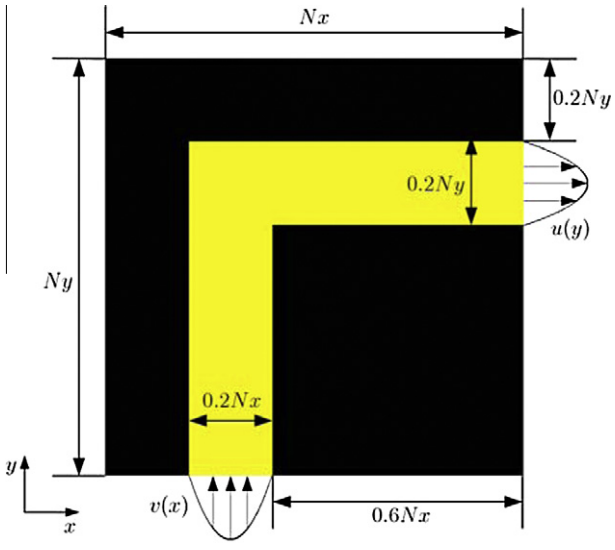

Fig. 5. Initial design domain for flow through a two-dimensional right angle elbow.

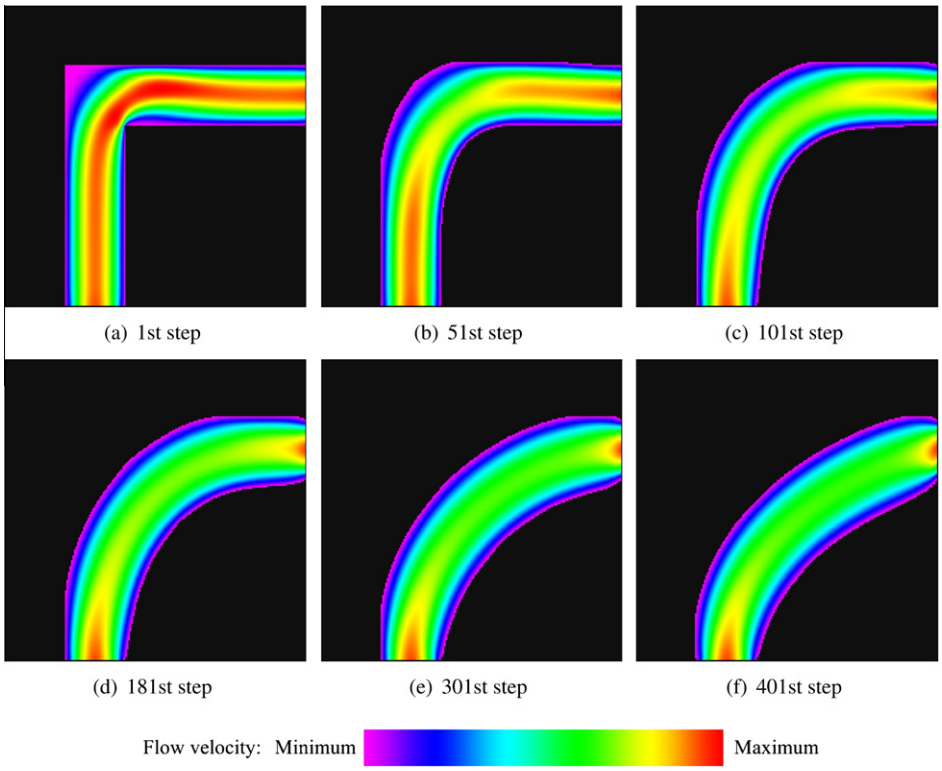

Fig. 6. Shape and flow field evolution from first to the 401st step for $Re = 40$ flow through a right angle elbow.

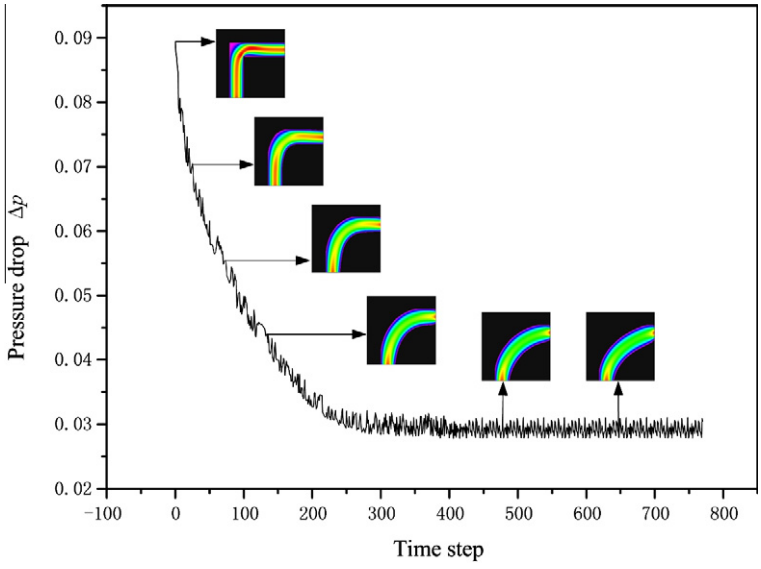

Fig. 7. The evolution of total pressure drop with time steps for $Re = 40$ flow through a right angle elbow.

that the singular pressure drop is dominant even under very low Reynolds number condition. This observation is consistent with the results reported by Tondeur and his coworkers [2,32]. However, it should be noted that the percentage of improvement is rather relative to some extent since it depends strongly on the choice of the initial shape.

The number of LBM iterations taken till the convergence criterion with time steps is shown in Fig. 8. It can be observed that the number of LBM iterations depends on the shape of fluid flow. The number of LBM iterations fluctuatly increases

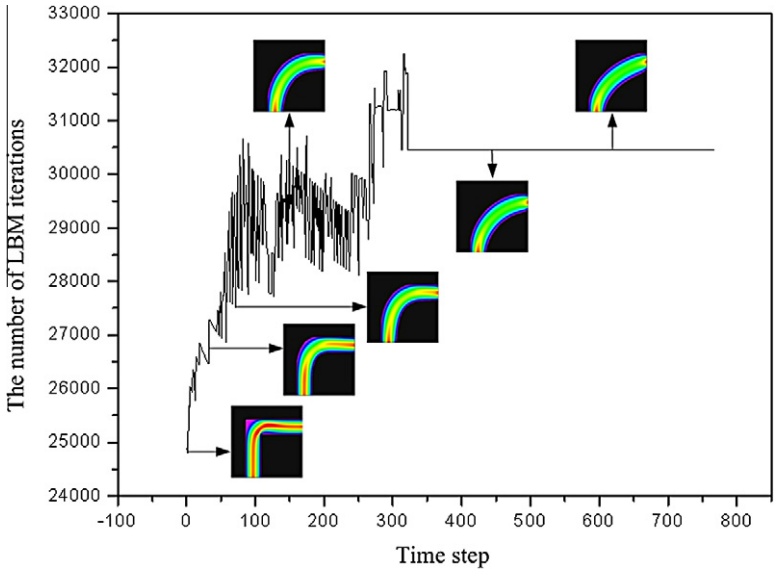

Fig. 8. The evolution of the number of LBM iterations with time steps for *Re* = 40 flow through a right angle elbow.

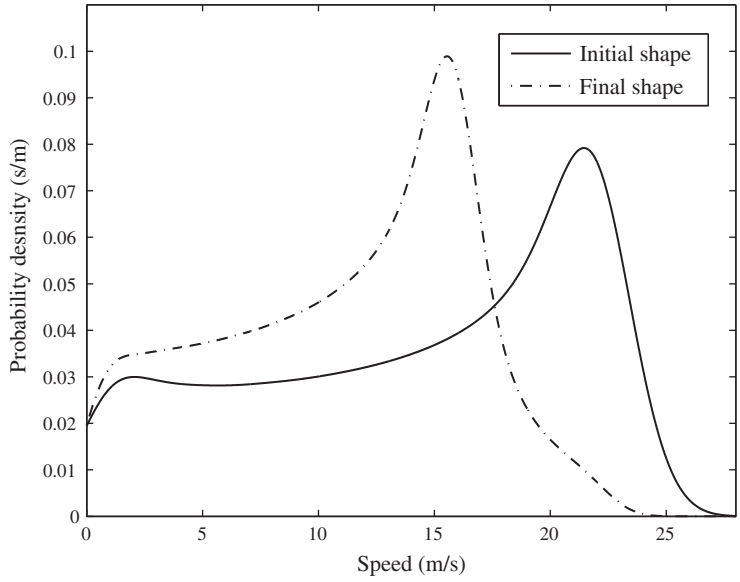

* The speed of sound $(c_s = 1/\sqrt{3})$ in D2Q9 LBM is supposed to be 327.19 m/s

Fig. 9. Comparison of the probability density functions of fluid speed for *Re* = 40 flow through a right angle elbow.

when the shape of fluid flow evolves with increasing time step, and tends to be stable after having been increased to a certain level. The average number of LBM iterations is approximately 30,500 once the final shape has been found.

In the mean time, it can also be observed from Fig. 6 that "dead zones" in the flow domain are largely eliminated at the final shape. One important feature related to this is the narrow residence time distribution which is essential for chemical reactors and fluid mixers for example. Fig. 9 shows the probability density as a function of fluid speed in the flow domain. Compared to the initial shape, a more narrow fluid speed distribution is obtained at the final shape, which shows that the flow field becomes more uniform.

We attempt to verify the present heuristic algorithm through comparison with several established topology optimization for Stokes flow [11] and channel flow [13,15,16], which will demonstrate the algorithm's ability for accurate shape design in fluid flow. Fig. 10 shows the final shapes at various Reynolds numbers (*Re* = 0.0267, 20, 40 and 80). As shown in Fig. 10(a), the right angle elbow finally evolves into a straight-pipe at *Re* = 0.0267 Stokes flow, which is

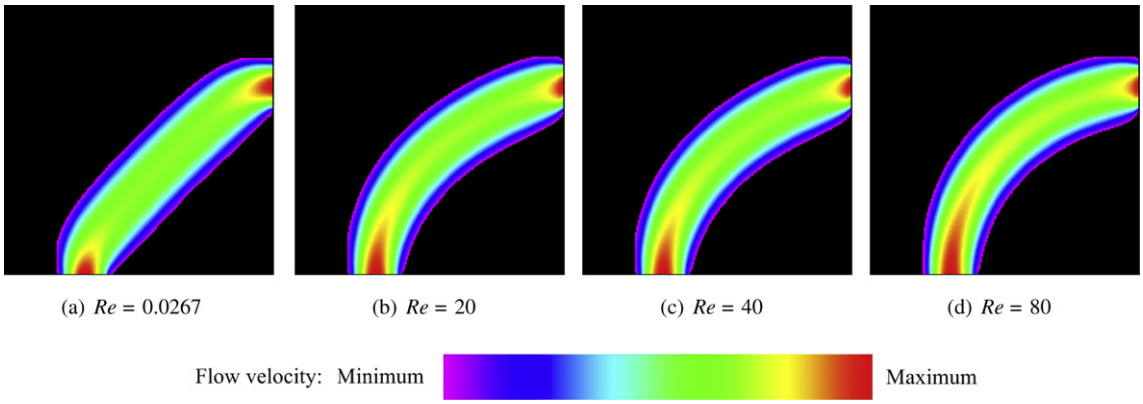

Fig. 10. Final shapes at various Reynolds for flow through a right angle elbow.

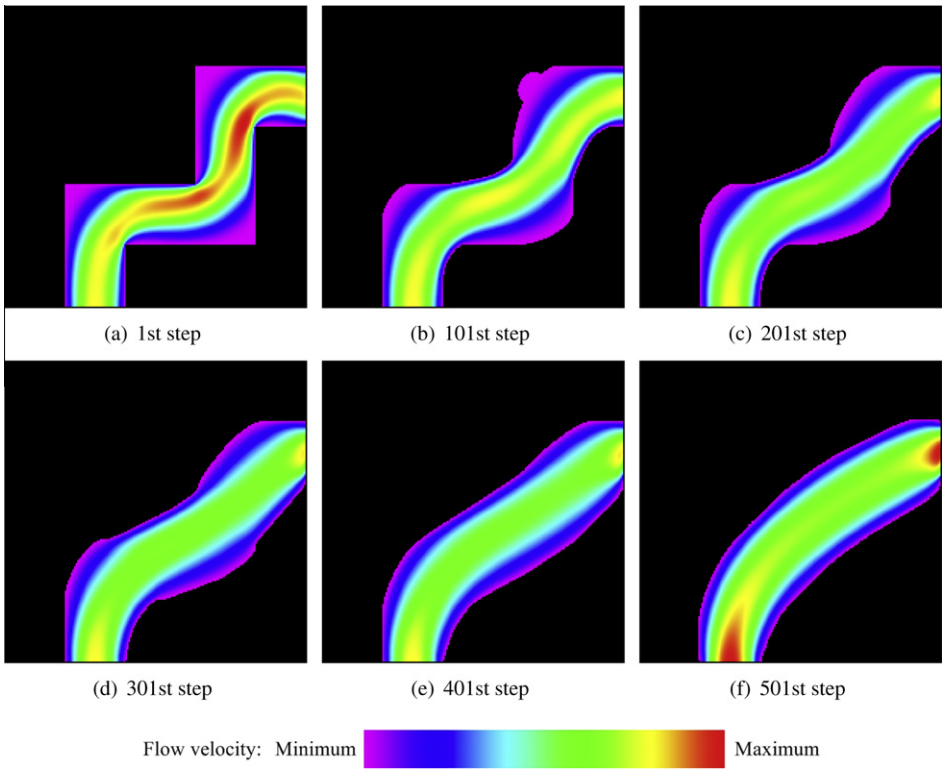

Fig. 11. Shape and flow field evolution from first to the 401st step for $Re = 40$ flow through a zigzag elbow.

close to the optimal results of Borrvall and Petersson [11]. In addition, Fig. 10 illustrates the influence of the Reynolds numbers on the final shapes. The larger the Reynolds number is (but restricted to pure laminar flow condition), the more curved in turn a corner of the pipe.

In order to investigate the influence of the initial shape, a comparative test is carried out, as shown in Fig. 11. Compared to the right angle elbow case, all the boundary conditions and physical properties for fluid flow are equal except the initial shape (zigzag in this case). It can be observed that by applying our algorithm, nearly (but not exactly) the same final configuration can be obtained, implying that our algorithm may not be sensitive to the choice of the initial shape in the current case investigated.

Furthermore, to assess the scalability/practicality of the present algorithm for lattice of realistic sizes, a comparative test regarding the "resolution" of the simulated domain has been carried out. We have investigated three lattice sizes (100×100; 200×200; 400×400) of the elbow case, while keeping other numerical parameters identical. Fig. 12 shows that almost identical final shapes are obtained, which suggests that the resolution of the flow domain has little influence on the final

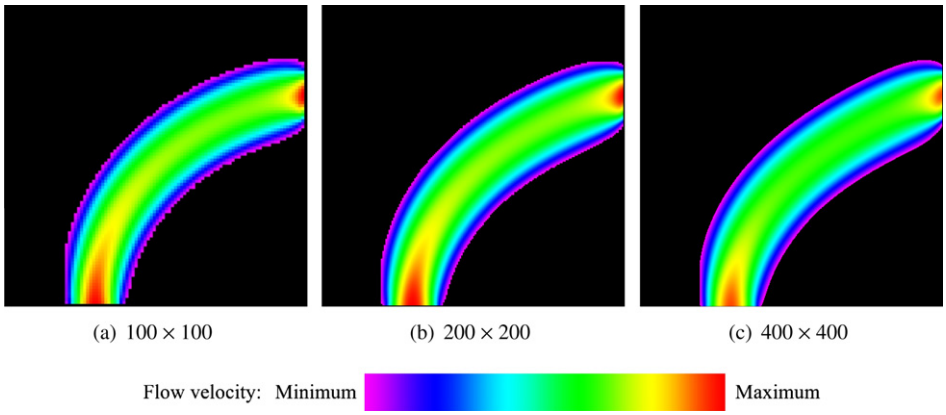

Fig. 12. The final shape of three lattice sizes for $Re = 40$ flow through a right angle elbow.

shape of the elbow. One feature that may be observed by comparing these pictures is that the boundary of the flow domain becomes smoother when the "resolution" increases. Another feature is that the small size converges much faster than the large size, i.e. about 200 iterations for 100×100 case, 380 iterations for 200×200 case and more than 550 iterations for 400×400 case. So as to the number of LBM iterations per optimization iteration change, the difference is also significant: less than 8000 for 100×100 case and about 45,000 for 400×400 case.

To further improve the efficiency of our algorithm, we may consider using a "multi-scale modeling" technique. That is, first calculate a rough shape using small lattice size and then progressively refine the flow domain in order to reach the acceptable resolution. This will be the subject of our future work.

3.2. T-junction flow

The initial profile of a *T*-junction merging flow which is widely used in engineering is shown in Fig. 1. The simulation domain is divided into 201×202 cells. The width of inlet boundary W_{in} is 35 cells and the width of outlet boundary W_{out} is 53

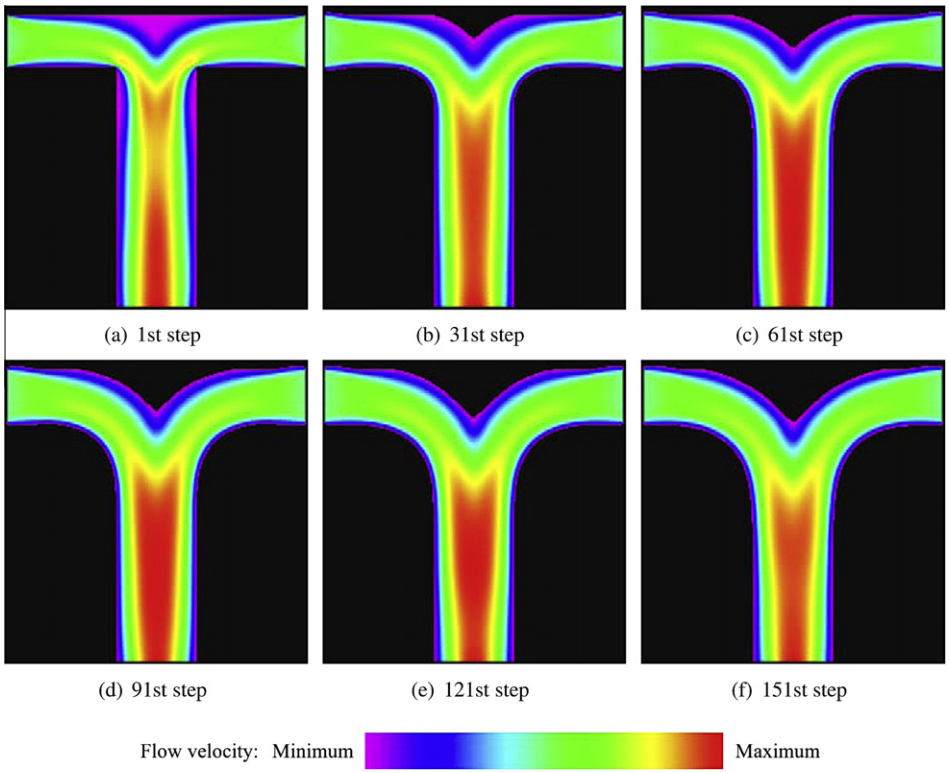

Fig. 13. Shape and flow field evolution from first to the 151st step for $Re_{out} = 17.5$ *T*-junction flow.

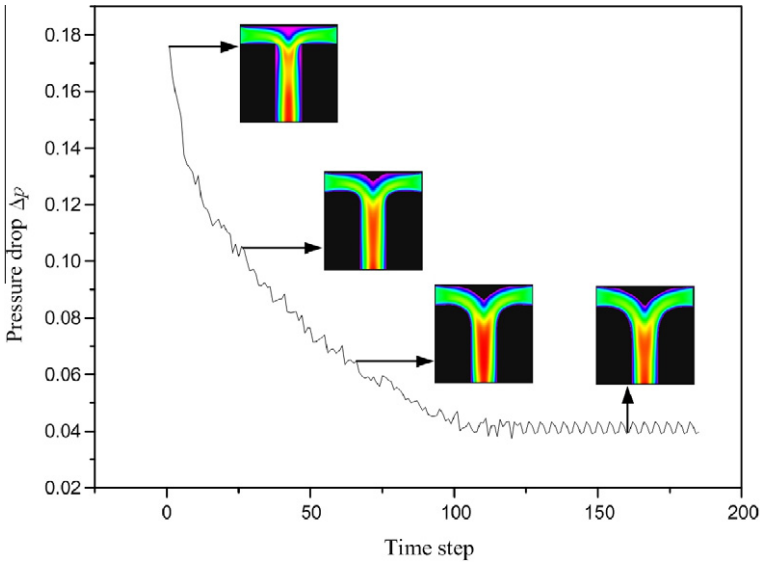

Fig. 14. The evolution of the total pressure drop with time steps for Re_{out} = 17.5 *T*-junction flow.

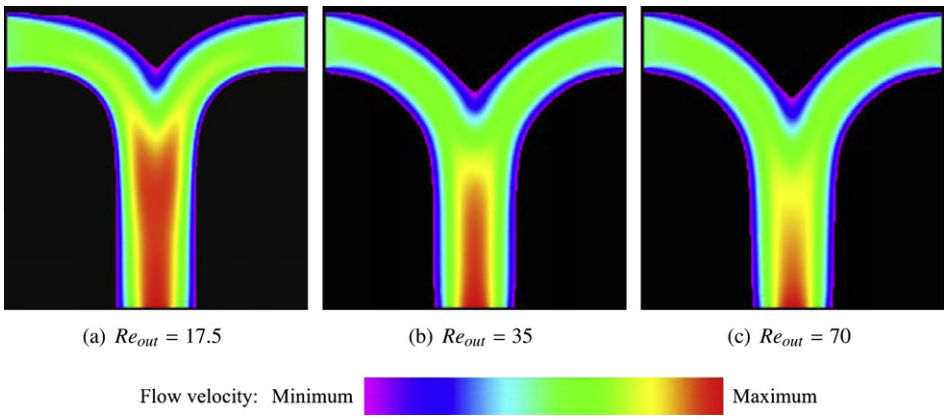

Fig. 15. Final shapes at various Reynolds for *T*-junction flow.

cells. Both right and left inlets have identical constant velocity profiles, but with opposite directions. A parabolic velocity profile at the outlet is imposed. The cross-sectional average fluid velocities of the outlet are $\bar{u}_{out} = 0.0132,\ 0.0264$ and 0.0528, the corresponding outlet Reynolds numbers $Re_{out} = \frac{\bar{u}_{out} W_{out}}{\nu} = 17.5, 35$ and 70. The constant inlet velocities are u_{in} = 0.01, 0.02 and 0.04, respectively.

Fig. 13 shows the shape evolution of the *T*-junction and the corresponding flow field as a function of the evolution time steps. It can be observed that the two right angels' corners gradually disappear and become circular transitions, while fluid cells having low dynamic pressure where two fluids join up are replaced by solid cells. Thus, the dead zones in the *T*-junction are largely eliminated, i.e. the void volume of the junction for fluid flow is more effectively "used". Finally, the *T*-junction evolves into a *Y* shape junction with natural and developed flow velocity field, which also implies that the mean residence time distribution is more uniform.

Fig. 14 reports the total pressure drop between the inlets and the outlet as a function of the evolution time step. It can be observed that the total pressure drop of the initial shape is 0.176, that of the final shape is 0.042, and the total pressure drop decreases when the algorithm proceeds. The total pressure drop of the final shape is reduced by 76.1% compared with that of the initial shape.

Fig. 15 illustrates the influence of the Reynolds numbers on the final shapes for *T*-junction flow. Based on these results, it can be seen that the final shapes of *T*-junction are similar at low Reynolds numbers. In Fig. 16 we plot the wall boundaries for Re_{out} = 17.5, 35 and 70. The observed slight decrease of the curvature at the two corners and top solid boundary gradually descends for larger Reynolds numbers.

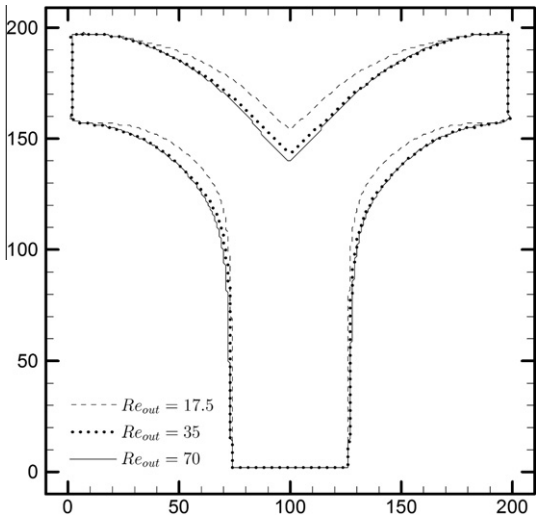

Fig. 16. Comparison the final outlines of *T*-junction at Re_{out} = 17.5, 35 and 70.

4. Discussion and conclusions

A heuristic optimality criterion algorithm for shape design of fluid flow based on LBM is proposed in this paper. With constant void volume constraint, the algorithm mainly exchanges the positions of solid cells suffering high viscous stress with fluid cells having low dynamic pressure at fluid–solid interface. Step by step, the shape of fluid flow evolves toward the final shape with reduced pressure drop. Two simple examples are illustrated: one is a right angle elbow and the other a converging *T*-junction. Encouraging results are obtained, illustrating the validity of algorithm and its promising application in engineering field dealing with fluid problems.

The objective of the present study is to minimize the pressure drop under the constraint of constant void volume for fluid flow. In fact, the minimization of pressure drop is equal to the minimization of viscous dissipation, or the entropy generation under isothermal condition, thus our method can also be considered as Entropy Generation Minimization (EGM) [33] from view point of thermodynamics.

The heuristic optimality criteria chosen in this algorithm are the viscous stress for solid cells and the dynamic pressure for fluid cells, corresponding to the physical mechanism at fluid–solid interface. In fact, considering a mighty wave crashing on a sandy shore as a typical fluid–solid interaction example, the solid elements are more likely to collapse when they suffer high viscous stress, beyond the fracture threshed, thus will be eroded by fluids. Meanwhile, the fluids having small velocity (low dynamic pressure) are more likely to be occupied by solid. That's how the shape of a river evolves subject to its local and global constraints in nature. Indeed, other optimization criteria may also be valid for dealing with specific problems under specific conditions.

Two simple examples illustrated in this paper are under low Reynolds number, incompressible flow conditions (pure laminar flow). This is because of the assumption of low Mach number in current D2Q9 model of LBM. However, the present algorithm can also be extended to tackle more complicated flow problems such as developed turbulent flow or compressible flow, by selecting and integrating proper models. This is one direction of our future work.

For a "closer to nature" analysis, a three-dimensional simulation is necessary for comparing the effects of different channel section geometries on the optimization results. For simplicity of implementation, the current simulation scheme lies in the restriction of two-dimensional surface, the height of channel is assumed infinite. However, its extension to three-dimensions is in principle straightforward. This is technically feasible by the three-dimensional lattice Boltzmann models (D3Q15, D3Q19 and D3Q27) [34,35], i.e. by dividing a volume space into a large number of elemental sub-cubes and using a modified macroscopic velocity expression.

It should be clarified that the solution generated by the present heuristic algorithm does not rigorously lead to a minimal flow resistance (pressure drop), since the optimality of the designs can not be properly assessed. It should also be noted that the proposed algorithm is unable to generate new boundaries, unless two existing boundaries accidentally merge during the optimization process, which could be considered as a drawback when compared with topology optimization.

Even with these limitations, the present heuristic algorithm avoids the need for costly sensitivity analysis required by traditional optimization and the present results seem reasonable and encouraging. Our next step is to apply this algorithm for the shape designs of more complex fluid flow structures, for example the multi-scale fluid distributors/collectors [2,4,32]. Experimental validation is also expected for this algorithm.

One assumption used in the present algorithm is that the whole operation is carried out under isothermal condition. This assumption is totally reasonable for our cases examined in this study, but may not be valid when physical properties of

working fluid are temperature dependent. Furthermore, when we design the fluid flow structures for actual engineering applications, i.e., heat exchangers or solar collectors, the thermal aspect is obviously not negligible. Therefore, it concerns the design and optimization of fluid flow structures expecting optimal thermal performance with minimal flow resistance simultaneously. In that case, other heuristic optimality criteria should be introduced, such as the local heat transfer coefficient or Nusselt number for fluid cells. In fact, we have had some successful attempts in dealing with pure heat conduction problem by using similar "position exchange" principle [36,37]. Developing a conjugate algorithm for both fluid flow and heat transfer to tackle the convective heat transfer problem is surely another direction of our future work.

Acknowledgments

This work has been done thanks to the facilities offered by the Université de Savoie Computing Center MUST. The authors wish to express their gratitude to Dr. Raphaël Boichot, Science et Ingénierie des Matériaux et Procédés (SIMaP), Grenoble INP-Phelma, for illuminative discussion. The authors also wish to thank the reviewers for their careful, unbiased and constructive suggestions.

References

[1] X. Wang, M. Damodaran, Aerodynamic shape optimization using computational fluid dynamics and parallel simulated annealing algorithms, AIAA Journal 39 (8) (2001) 1500–1508.
[2] D. Tondeur, L. Luo, Design and scaling laws of ramified fluid distributors by the constructal approach, Chemical Engineering Science 59 (8–9) (2004) 1799–1813.
[3] L. Luo, Y. Fan, W. Zhang, X. Yuan, N. Midoux, Integration of constructal distributors to a mini crossflow heat exchanger and their assembly configuration optimization, Chemical Engineering Science 62 (13) (2007) 3605–3619.
[4] Y. Fan, R. Boichot, T. Goldin, L. Luo, Flow distribution property of the constructal distributor and heat transfer intensification in a mini heat exchanger, AIChE Journal 54 (11) (2008) 2796–2808.
[5] O. Moos, F. Klimetzek, R. Rossmann, Bionic optimization of air-guiding systems, Proceedings of SAE 2004 World Congress & Exhibition, Society of Automotive Engineering, Detroit, MI, USA, 2004, pp. 95–100.
[6] F. Klimetzek, J. Paterson, O. Moos, Autoduct: topology optimization for fluid flow, in: Proceedings of Konferenz fur Angewandte Optimierung, Karlsruhe, 2006.
[7] A. Jameson, Aerodynamic design via control theory, Journal of Scientific Computing 3 (3) (1988) 233–260.
[8] A. Bejan, Shape and Structure, from Engineering to Nature, Cambridge University Press, 2000.
[9] B. Mohammadi, O. Pironneau, Shape optimization in fluid mechanics, Annual Review of Fluid Mechanics 36 (2004) 255–279.
[10] M. Gunzburger, Perspectives in Flow Control and Optimization, Society for Industrial Mathematics, Philadelphia, PA, 2003.
[11] T. Borrvall, J. Petersson, Topology optimization of fluids in Stokes flow, International Journal for Numerical Methods in Fluids 41 (1) (2003) 77–107.
[12] A. Evgrafov, The limits of porous materials in the topology optimization of Stokes flows, Applied Mathematics and Optimization 52 (3) (2005) 263–277.
[13] A. Gersborg-Hansen, O. Sigmund, R. Haber, Topology optimization of channel flow problems, Structural and Multidisciplinary Optimization 30 (3) (2005) 181–192.
[14] A. Evgrafov, Topology optimization of slightly compressible fluids, Zeitschrift fur Angewandte Mathematik und Mechanik 86 (2005) 46–62.
[15] A. Evgrafov, G. Pingen, K. Maute, Topology optimization of fluid problems by the lattice Boltzmann method, Solid Mechanics and its Applications 137 (2006) 559–568.
[16] G. Pingen, A. Evgrafov, K. Maute, Topology optimization of flow domains using the lattice Boltzmann method, Structural and Multidisciplinary Optimization 34 (6) (2007) 507–524.
[17] X. Duan, Y. Ma, R. Zhang, Shape-topology optimization for Navier–Stokes problem using variational level set method, Journal of Computational and Applied Mathematics 222 (2) (2008) 487–499.
[18] S. Zhou, Q. Li, A variational level set method for the topology optimization of steady-state Navier–Stokes flow, Journal of Computational Physics 227 (24) (2008) 10178–10195.
[19] U. Frisch, B. Hasslacher, Y. Pomeau, Lattice-gas automata for the Navier–Stokes equation, Physical Review Letters 56 (14) (1986) 1505–1508.
[20] G. McNamara, G. Zanetti, Use of the Boltzmann equation to simulate lattice-gas automata, Physical Review Letters 61 (20) (1988) 2332–2335.
[21] Y. Qian, D. d Humières, P. Lallemand, Lattice BGK models for Navier–Stokes equation, Europhysics Letters 17 (6) (1992) 479–484.
[22] R. Benzi, S. Succi, M. Vergassola, The lattice Boltzmann equation: theory and applications, Physics Reports 222 (3) (1992) 145–197.
[23] X. He, L. Luo, Lattice Boltzmann model for the incompressible Navier–Stokes equation, Journal of Statistical Physics 88 (3) (1997) 927–944.
[24] S. Chen, G. Doolen, Lattice Boltzmann method for fluid flows, Annual Review of Fluid Mechanics 30 (1) (1998) 329–364.
[25] S. Succi, The Lattice Boltzmann Equation for Fluid Dynamics and Beyond, Oxford University Press, 2001.
[26] S. Wolfram, Statistical mechanics of cellular automata, Reviews of Modern Physics 55 (3) (1983) 601–644.
[27] T.L. Anderson, Fracture Mechanics: Fundamentals and Applications, CRC Press, 2005.
[28] S. Chen, D. Martinez, R. Mei, On boundary conditions in lattice Boltzmann methods, Physics of Fluids 8 (1996) 2527–2536.
[29] Q. Zou, X. He, On pressure and velocity boundary conditions for the lattice Boltzmann BGK model, Physics of Fluids 9 (1997) 1591–1598.
[30] L. Wang, W. Ge, J. Li, A new wall boundary condition in particle methods, Computer Physics Communications 174 (2006) 386–390.
[31] W. Ge, F. Chen, J. Gao, et al, Analytical multi-scale method for multi-phase complex systems in process engineering-bridging reductionism and holism, Chemical Engineering Science 62 (13) (2007) 3346–3377.
[32] D. Tondeur, Y. Fan, L. Luo, Constructal optimization of arborescent structures with flow singularities, Chemical Engineering Science 64 (18) (2009) 3968–3982.
[33] A. Bejan, Entropy Generation Minimization: The Method of Thermodynamic Optimization of Finite-size Systems and Finite-Time Processes, CRC Press, 1996.
[34] S. Chen, Z. Wang, X. Shan, G. Doolen, Lattice Boltzmann computational fluid dynamics in three-dimensions, Journal of Statistical Physics 68 (3) (1992) 379–400.
[35] D. d'Humières, I. Ginzburg, M. Krafczyk, P. Lallemand, L. Luo, Multiple-relaxation-time lattice Boltzmann models in three-dimensions, Philosophical Transactions of the Royal Society A 360 (2002) 437–451.
[36] R. Boichot, L. Luo, Y. Fan, Tree-network structure generation for heat conduction by cellular automaton, Energy Conversion and Management 50 (2) (2009) 376–386.
[37] R. Boichot, L. Luo, A simple cellular automaton algorithm to optimize heat transfer in complex configurations, International Journal of Exergy 7 (1) (2010) 51–64.